Thermoacoustic ultrasound assessment of liver steatosis - a novel approach for MASLD diagnosis

Short title: Thermoacoustic Ultrasound Assessment of Liver Steatosis

Manuscript category: Original Research

Authors: Jang Hwan Cho[1], Christopher Bull[1], Michael Thornton[1], Jing Gao[2], Jonathan M. Rubin[3], Idan Steinberg[1,*]

Affiliations:
1 - ENDRA Life Sciences Inc., Ann Arbor, MI 48105, USA

2 - Department of Clinical Sciences, Rocky Vista University, Montana College of Osteopathic Medicine, Billings, MT, USA

3 - University of Michigan Department of Radiology, Ann Arbor, Michigan, USA

* - corresponding author.
Contact details:
Name: Idan Steinberg, Ph.D.
Affiliation: Vice President for Research and Development, ENDRA Life Sciences Inc
Address: 3600 Green Court, Suite 350, Ann Arbor, MI 48105-2240
Phone: *734.968.9538*
Mail: *isteinberg@endrainc.com*

Abstract

Metabolic Dysfunction-Associated Steatotic Liver Disease (MASLD) is a global health crisis, but current diagnostics are limited. Liver biopsy is invasive, magnetic resonance imaging-proton density fat fraction (MRI-PDFF) is expensive, and quantitative ultrasound methods are low-accuracy, especially in patients with a high body mass index (BMI). This study introduces a novel thermo-acoustic (TA) method that generates ultrasound signals based on tissue electrical conductivity, where lean tissue (high in water and electrolytes) absorbs more radio-frequency (RF) energy than fatty tissue, providing a direct molecular contrast for fat. This prospective, cross-sectional feasibility study compared a new thermo-acoustic fat fraction (TAFF) score with the reference standard MRI-PDFF in 40 participants with suspected fatty liver disease. The study population was obese (mean BMI 33.3 kg/m²). TAFF estimates demonstrated a substantial (89%) correlation with MRI-PDFF and an average absolute error of 3.04% fat fraction. Classification performance was high, with an AUROC of 0.92 at the 12% fat fraction threshold and 0.99 at the 20% fat fraction threshold. Critically, estimation errors showed no statistically significant correlation with BMI or other body habitus measurements. Overall, the feasibility study suggests that TAFF can be used accurately to quantify liver fat across the full MASLD spectrum, with predictive values closely aligned with those of MRI-PDFF, thereby enabling assessment, diagnosis, and monitoring of MASLD. These findings support thermoacoustics' potential as an accurate, non-invasive, point-of-care solution that could address the cost and access constraints of MRI and the limitations of current quantitative ultrasound methods.

***Keywords**: Area under ROC; hepatic steatosis; magnetic resonance imaging; metabolic dysfunction-associated steatotic liver disease; thermoacoustic; ultrasound*

Introduction

Clinical background

Metabolically dysfunction-associated steatotic liver disease (MASLD), formerly known as nonalcoholic fatty liver disease (NAFLD), is a complex, multi-system metabolic disorder characterized by elevated liver fat fraction (LFF). The steatotic liver is not passive; it acts as an active endocrine organ, secreting hepatokines such as Fetuin-A that drive systemic insulin resistance and chronic inflammation through a vicious cycle of lipotoxicity and oxidative stress [1–11]. This metabolic cascade has profound systemic implications, such as cardiovascular disease (CVD) [12], type 2 diabetes (T2D) [13], hypertension, and neurodegenerative diseases [14]. Recently, MASLD has emerged as a global health crisis, with an estimated prevalence of approximately 30%, establishing MASLD as the most common chronic liver disease in Western nations [15–17].

An estimated 20-30% of individuals with MASLD develop metabolic dysfunction-associated steatohepatitis (MASH), characterized by inflammation and fibrosis that places them at high risk for severe morbidity [18]. This disease progression is clinically significant as MASH is a leading driver for the development of cirrhosis, hepatocellular carcinoma (HCC), liver failure, and ultimately liver transplantation [19,20]. Furthermore, MASLD is strongly associated with a complex of chronic diseases that extend beyond the liver, with CVD representing the primary cause of mortality in the MASLD patient population [12]. However, this risk is dynamic rather than static, as clinical evidence shows that reversing hepatic steatosis successfully ameliorates systemic dysfunction and significantly reduces the risk of associated cardiovascular events [21–25].

Historically, the management of MASH has been predicated upon lifestyle modifications, primarily focused on inducing sustained weight loss [26]. The therapeutic landscape, however, is undergoing a rapid and profound transformation. This evolution was dramatically underscored by the 2024 landmark FDA approval of the first MASH-specific pharmacotherapy, Resmetirom (being marketed as Rezdiffra) [27]. In parallel, robust Phase 3 clinical trial data have demonstrated the compelling efficacy of various incretin therapies, including Glucagon-like Peptide-1 receptor agonists (GLP-1 RAs) such as semaglutide. These agents exhibit high rates of MASH resolution and marked improvements in hepatic fibrosis, firmly establishing them as a cornerstone of future metabolic-based therapeutic strategies [28]. And because MASLD patients die primarily from CVD, GLP-1 RAs offer crucial extrahepatic benefits that target these metabolic complications. Patients with MASLD and coexisting type 2 diabetes, GLP-1 RAs are associated with a significantly lower incidence of major adverse cardiovascular events and all-cause mortality compared to other glucose-lowering drugs[29–31].

Current diagnostic methods for steatotic liver disease exhibit a clear hierarchy based on their accuracy and clinical application. Liver biopsy remains the only definitive method for diagnosing

MASH by identifying characteristic inflammation and ballooning; however, its utility for precise, longitudinal quantification is significantly limited by its invasiveness, substantial cost, high risk of sampling error, and inherent inter-observer variability [32,33]. In contrast, magnetic resonance imaging-proton density fat fraction (MRI-PDFF) has emerged as the non-invasive reference standard for quantifying hepatic fat, demonstrating high accuracy and reproducibility, thereby establishing it as the preferred modality for clinical trials [34,35]. Positioning itself as a widely accessible screening method, the first-generation quantitative ultrasound tool, the controlled attenuation parameter (CAP), offers adequate diagnostic accuracy. However, its performance is known to be confounded by factors such as high body mass index (BMI) [36–38]. This emphasis on objective measurement is mandated by the 2025 American Association for the Study of Liver Diseases (AASLD) guidance, which explicitly recommends quantitative methodologies, such as CAP or MRI-PDFF, over standard, subjective gray-scale ultrasound for detecting steatosis [39].

MASLD diagnosis

The most recent advancements involve state-of-the-art Quantitative Ultrasound (QUS) techniques that leverage advanced analysis of beamformed images or raw radiofrequency ultrasound signals to assess complementary acoustic properties [40–42]. The attenuation coefficient (AC) provides a quantitative measure of the rate of energy loss of the ultrasound beam as it propagates through the hepatic parenchyma [43]. The backscatter coefficient (BSC) measures the energy scattered back to the ultrasound transducer, a phenomenon strongly influenced by the accumulation of intracellular lipid droplets, which act as acoustic scatterers and alter tissue physical organization [44]. Ultrasound-derived fat fraction (UDFF) represents the most advanced QUS modality, integrating both AC and BSC into a robust algorithm. Head-to-head comparisons have consistently demonstrated that UDFF offers superior accuracy compared to the earlier CAP method [45,46].

While quantitative ultrasound methods for liver fat assessment, such as the controlled attenuation parameter (CAP), UDFF, and ultrasound-guided attenuation parameter (UGAP), offer non-invasive approaches to assess hepatic steatosis, they show substantially reduced performance in individuals with elevated BMI. UGAP, for example, demonstrates markedly lower accuracy for diagnosing severe steatosis (S3) in subjects with BMI > 30 kg/m² [47]. These BMI-associated limitations arise from increased skin-to-capsule distance that degrades acoustic signal quality [12], depth-dependent variability in measurement thresholds, and anthropometric factors that independently affect whether CAP measurements achieve acceptable interquartile ranges [48]. Additional BMI-related tissue characteristics further impair liver fat quantification for these techniques: Karlas et al. [49] described “muscular viscoelastic adaptations” in overweight individuals that alter acoustic propagation, and Maar et al. showed that hepatic imaging quality decreases with increasing BMI. However, high-performance probes can partially mitigate this effect [50]. Consistent with these findings, Cusi et al. [51] reported that ultrasound

exhibits low sensitivity for detecting hepatic steatosis in obese and severely obese patients. Depth dependence compounds these challenges, as a retrospective study of AC algorithms from Canon, Philips, and Siemens demonstrated a progressive decline in AC values with increasing measurement depth, as well as significantly higher values with a 1 cm ROI compared with a 3 cm ROI [44]. Collectively, these BMI- and depth-related constraints highlight the need for standardized acquisition protocols and improved quantitative ultrasound approaches capable of producing accurate and reliable liver fat measurements across diverse body habitus.

While the prevalence and related morbidity of MASLD, in combination with the introduction of new treatment options such as GLP-1 drugs, necessitate screening and monitoring of a broad population [52], none of the abovementioned methods is suitable for such a task. Invasive biopsies are painful, costly, and introduce a non-negligible risk to patients [32]. While MRI-PDFF is accurate and non-invasive [34], it is cost-prohibitive and cannot be performed at the bedside. Ultrasound-based methods, albeit low cost and portable, often suffer from low predictive power, especially in patients with high BMI or confounding fibrosis due to reliance on surrogate parameters in place of fatty tissue molecular contrast. Thus, there is an unmet clinical need for a non-invasive, low-cost, rapid, and portable method with high predictive power for screening and monitoring MASLD treatment.

Thermoacoustic imaging

Thermoacoustic (TA) imaging is a hybrid electromagnetic (EM) and acoustic imaging modality that leverages differential absorption of time-varying EM radiation to generate pressure waves in tissue [53]. As the EM radiation propagates through the tissue, its energy is differentially absorbed by regions based on electrical conductivity [54–56]. This selective absorption results in a rapid, localized increase in temperature. Although the temperature rise is minuscule - often on the order of milliKelvins (mK) - the almost instantaneous, localized change in tissue temperature is sufficient to generate an acoustic pressure wave that is detectable by an ultrasound transducer array. The wave intensity is proportional to the tissue conductivity, thus providing molecular contrast [57]. The detected pressure signals can then be used to reconstruct images or volumes of data related to tissue composition [58].

Currently, most academic research focuses on system engineering [59–61] or pre-clinical imaging, such as functional brain imaging and cerebral hemorrhage detection [62] or joint and bone imaging [63]. Other examples include deep-tissue (>6 cm) kidney imaging in large swine and real-time monitoring of therapeutic interventions, such as microwave ablation (MWA) therapy [64]. However, in recent years, TA imaging has emerged as a clinical tool for diagnosing and monitoring various tissues and disease states. For example, in their seminal paper, Kruger et al. [65] demonstrated clear contrast enhancement in the tumor region for three patients imaged both before and after chemotherapy. Conversely, the two breast cancer patients imaged after completing their chemotherapy showed no contrast enhancement. This finding correlated with

subsequent pathologic examinations, which confirmed their disease was in complete remission. More recently, Scott et al. utilized thermo-acoustic ultrasound [66] as a pre-scan procedure to assess the risk of potentially hazardous RF-induced heating at the tips of implanted medical device leads during MRI scans. This difficulty currently restricts many patients from receiving MRIs. The authors developed a system, integrated it with an MRI scanner, and successfully detected a peak in RF power absorption near a model lead tip, the source of the heating.

This paper describes a system and a first-of-a-kind clinical study to assess the feasibility of a point-of-care, portable thermoacoustic system for liver fat fraction measurement. To that end, Endra Life Sciences, Inc. has developed a thermo-acoustic enhanced ultrasound system (TAEUS® Liver) that combines RF-based MRI-PDFF-like contrast mechanism with the low cost and portability of ultrasound [67]. TA techniques are quintessential for estimating liver fat, as the contrast mechanism relies on differences in tissue conductivity when subjected to an RF pulse: lean tissues, which have high water and ion content, absorb significantly more energy than fatty tissues, which have low water and ion content. This difference in energy absorption, particularly at the boundary between muscle and the liver, generates a stronger thermoacoustic signal as the liver's fat content increases, enabling quantitative measurement of steatosis. Moreover, the layered structure of the tissue (skin, subcutaneous fat, muscle, and then liver) provides an inherent calibration method for the measured signal, as subcutaneous fatty tissue is predominantly fat (>90%) and muscle is predominantly lean tissue (>95%). Thus, for each measurement, signals from purely fatty and purely lean tissues are acquired along with the unknown liver tissue, allowing them to be used for calibration. The remainder of the paper describes the clinical trial evaluating the performance of this method compared to the reference standard MRI-PDFF.

Materials and Methods

TAEUS® Liver system

The TAEUS® Liver System (Endra Life Sciences, Inc., Ann Arbor, Michigan, USA) is a point-of-care thermoacoustic system for measuring LFF. It includes four main subsystems, as illustrated in Figure 1A: (1) The TAEUS console: A cart-mounted enclosure that contains an RF Source, electronics, and software. (2) TAEUS probe: A handheld component that includes an RF applicator and a receive-only ultrasound transducer. (3) TAEUS display assembly: A touchscreen tablet that is the graphical user interface for the ultrasound probe, a touchscreen monitor (TA display) that is the graphical user interface and input device to the TAEUS® Liver System. (4) Handheld ultrasound probe: a wireless U/S probe. Figure 1B shows a photo of the system.

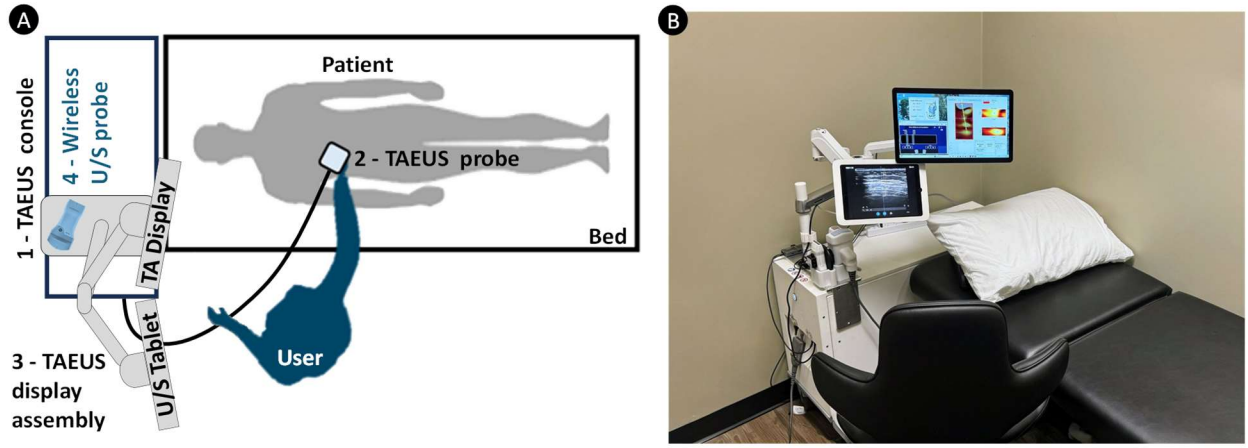

Figure 1 - The TAEUS Liver system (A) Illustration of the main subsystems of the TAEUS Liver System: (A.1) console, (A.2) TAEUS Probe, (A.3) Display assembly, (A.4) Wireless ultrasound probe. (B) a photo of the scanning room with the TAEUS Liver system

During a scan, the TAEUS console generates high-power RF pulses (7 kW peak power). It delivers these pulses to the RF applicator within the TAEUS Probe via a coaxial cable. The RF applicator is an open-ended waveguide antenna designed to couple RF energy into human tissue efficiently. Using an RF tap, a small fraction (<0.01%) of the power is redirected to a power monitor inside the console, ensuring every pulse is monitored for safety. The system operates below the specific absorption rate (SAR) limits for standard mode MRI operation [68] and below the maximal permissible exposure (MPE) for the electric field. [69].

The transducer within the TAEUS probe receives the ultrasound signal generated by the TA conversion of the RF pulse energy into acoustic energy. The ultrasound signal is then amplified, digitized, and sent to the TAEUS console for processing and subsequent display on the graphical user interface. A TA exam includes a few preview scans (i.e., 125 pulses each) to ensure that the TAEUS probe is adequately positioned and can pick a clear liver signal, followed by a longer one or more measurement scans (250 pulses each).

Both the preview and measure scans are processed in the same way. Acquired scan data are averaged and digitally filtered to reduce noise and artifacts. A Hilbert transform is applied to the filtered data, followed by universal back-projection [70] and envelope detection to generate the beamformed image. Since the TAEUS probe is handheld, its positioning and placement affect the quality of the acquired scan. To identify valid scans with features critical to the accurate thermo-acoustic fat fraction (TAFF) estimation, a scan-quality metric was designed and calculated for each scan. The scan quality metric comprises various geometric and image-based features to ensure that signals are free of interference and their locations are consistent with ultrasound imaging.

For each scan, the TAFF value is estimated from the corresponding beamformed image. Since the TAEUS probe was positioned so that the field of view includes skin, subcutaneous fat, muscle,

and liver, the beamformed image from that location is expected to show three signals: at the skin-to-subcutaneous fat boundary, the fat-to-muscle boundary, and the muscle-to-liver boundary. Based on these expected signals at the tissue boundaries, the TAFF estimation is formulated as an optimization problem that seeks the liver fat content by minimizing the difference between measured and theoretically expected signal strengths. The cost function relies on a thermoacoustic signal generation model incorporating various tissue properties, including the Grüneisen parameter, tissue permittivity, tissue electrical conductivity, and the subject-specific electric field distributions provided by our electric field model. The electric field model generated the necessary electric field distributions for subjects with various body habitus and liver fat content, and was estimated using Ansys HFSS (Ansys, Canonsburg, PA, USA) simulation software to account for these variations.

Study description

To assess TAEUS's ability to accurately estimate LFF across various disease states and body habitus, a prospective, HIPAA-compliant, cross-sectional study was conducted. A single US site (Ann Arbor, MI, USA) single operator study was approved by the Advarra Institutional Review Board (IRB approval number: Pro00089043). First, prospective participants recruited from the local population were screened via questionnaire for clinically proven or suspected elevated liver steatosis (based on known comorbidities, lifestyle, and body habitus). If liver steatosis was confirmed or suspected, participants were invited to join the study, and written informed consent was obtained. This was done primarily to increase the number of subjects with liver steatosis in the study and allow the TAEUS system to be tested across all disease grades. Inclusion and exclusion criteria are described in Table 1 below:

Table 1 - Study inclusion and exclusion criteria

Inclusion Criteria	Exclusion Criteria
● Over 18 years of age ● Able to provide informed consent ● Able to tolerate both an MRI and an ultrasound ● Ability to lie flat or on side for 20 minutes, and pause breathing for up to 10 seconds	● Metal or electronic implants that contraindicate MRI ● Known pregnancy on the day of consent or becoming pregnant during study participation, based on start date of last menstrual period ● BMI greater than 50 kg/m^2 ● Liver diseases other than MASLD/MASH/fibrosis, including, but not limited to, cirrhosis, hepatocellular carcinoma, and ascites ● Broken or injured skin in the right upper abdominal quadrant ● Body habitus, or anatomical variation, where the liver capsule is not accessible with ultrasound through the patient's right intercostal imaging window, used in conventional ultrasound liver imaging ● Subcutaneous fat at measurement location less than or equal to 6 mm ● Focal liver lesions or anatomical structures in the measurement location, as detected by ultrasound

- Missing liver lobe
- Peri-hepatic fat in the measurement location

Subjects with liver diseases other than steatosis, such as cancer or ascites, or abnormalities such as missing liver lobes, polycystic disease (multiple hepatic cysts) were excluded from the study to prevent potential confounding factors. Any subject with an obstruction that prevented imaging of the liver capsule through the right intercostal imaging window was also rejected to ensure adequate measurement of the liver. Subjects with perihepatic fat at the measurement site, as identified by ultrasound or MRI, were also excluded from the study, as the current TAEUS liver fat estimation algorithm assumes no perihepatic fat at that location. Finally, due to the low-frequency transducer (0.5 MHz) of the TAEUS probe, subjects with subcutaneous fat at the measurement location of less than or equal to 6 mm were also rejected, as this thin fatty layer produced poorly resolved signals at the fat-to-muscle boundary. A flowchart of the study is shown in Figure 2.

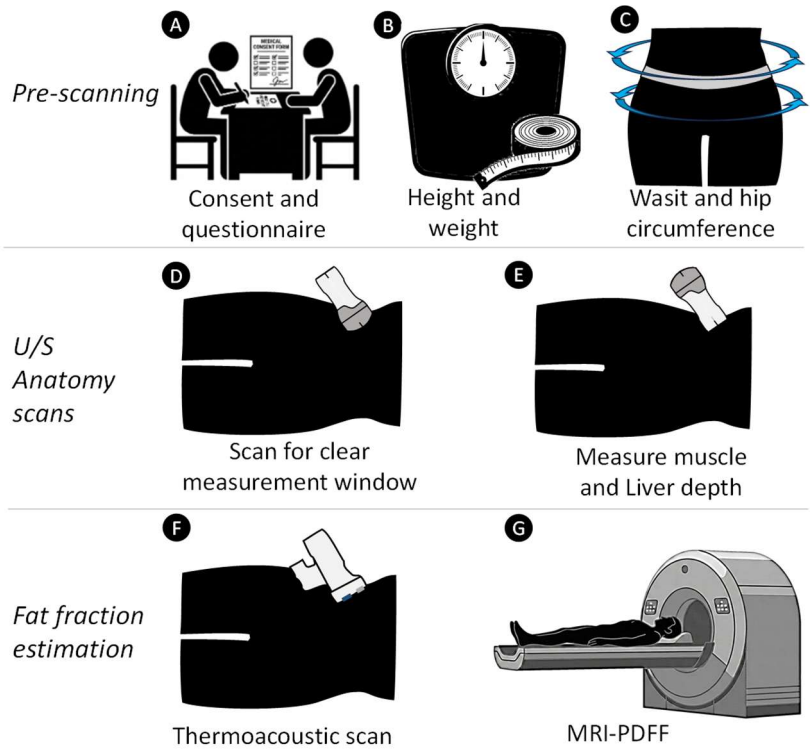

Figure 2 - Graphical description of clinical study. (A) Patients were first consented and their relevant medical history and demographics were recorded (B&C) Body habitus - weight, height, waist, and hip circumference were recorded (D) Curved array, wireless U/S scanner was used to locate a field of view clear of obstructions such as lung, bowel & perihepatic fat (E) Linear array U/S wireless U/S scanner was used to measure the depth of the subcutaneous fat to muscle boundary and the liver capsule boundary location (F) The TAEUS probe was used at the exact anatomic location to estimate the liver fat of each subject (G) Each subject was sent to a reference standard MRI-PDFF scan for recording the ground truth fat fraction.

Participants were instructed to fast for 4 hours prior to the ultrasound scan. The scan was performed on the participant in a slight (30 degrees) left lateral decubitus position, raising the right arm to extend the intercostal space. During a scanning session, the subject's anatomy was assessed using a wireless, handheld ultrasound system (Vscan Air™ CL, GE Health Care, Milwaukee, WI, USA). A liver window clear of obstructions was first identified with the curved-array side of the probe, after which the subcutaneous fat thickness and liver capsule depth were measured using the linear-array side. The measurement position was marked on the subject with a surgical marker, and the probe orientation was captured with a 9-axis Bluetooth inclinometer (WT901BLECL, WitMotion, Shenzhen, China). Subsequently, a TA scan was performed. A second inclinometer was attached to the TAEUS probe to ensure its orientation matched that of the ultrasound probe. The bedtime for the entire session was usually shorter than 10 minutes. TAEUS and MRI-PDFF evaluations were obtained within a four-week period to ensure the subject's liver fat did not change considerably. MRI-PDFF images were acquired on a 3.0-T MRI clinical scanner (Ingenia, Philips Healthcare, Netherlands). A three-plane localization gradient-echo sequence was first obtained, followed by an mDIXON-Quant sequence in a single breath hold, which automatically reconstructs the PDFF map. The sequence parameters were: 6 TEs (first TE 0.98 ms, delta TE 0.8 ms), TR 6.3 ms, flip angle 3°, parallel imaging SENSE factor 2, no signal averaging, matrix size 160×140, field-of-view (FOV) 400×350 mm, 77 slices, and slice thickness 3 mm. MRI-PDFF measurements were obtained from nine manually placed circular ROIs, one in each hepatic segment (I, II, III, IVa, IVb, V, VI, VII, and VIII), ranging from 78 mm^2 (~10 mm diameter) to 314 mm^2 (~20 mm diameter), while avoiding large blood vessels [71]. The mean PDFF of the nine ROIs was calculated for each scan.

Data analysis

Regression, area under the receiver operating characteristic curve (AUROC), and accuracy analyses were conducted to evaluate TAFF's performance relative to the reference standard MRI-PDFF, with each subject represented by a paired measurement (mean TAFF, mean MRI-PDFF). A Bland-Altman analysis [72] was used to visualize the agreement and distribution of measurement errors. As this clinical study is the first to utilize TAFF, the Bland-Altman plot was also used to identify and correct for measurement bias (i.e., the mean error). Following bias correction, a Deming regression analysis [73] was used to evaluate the relationship between the MRI-PDFF and TAFF estimates of the liver fat. Deming regression was chosen because it appropriately accounts for measurement error in both the reference and test methods, making it well-suited for equivalence testing across different methods. Unlike ordinary linear regression, which assumes the independent variable is measured without error, Deming regression provides an unbiased estimate of the relationship between two imperfectly measured variables. It is widely used in clinical and analytical method comparison and is recommended in several methodological guidelines [74].

To estimate the Deming regression line, the ratio of variances between TAFF and MRI-PDFF

measurements was required. Measurement variability was calculated from repeated measurements on multiple subjects. To avoid underestimating the variance of TAFF measurements, participants with only one valid scan were excluded from the average estimate (35 subjects). As MRI performance can vary across vendors and sites, a conservative approach was adopted, relying on the Radiological Society of North America - Quantitative Imaging Biomarkers Alliance (RSNA-QIBA) publication, which quantified MRI-PDFF's variance using phantom data [15,75]. These publications suggest a standard deviation of 1.67% for pt fat fraction, corresponding to a variance of 2.778. For living subjects, this variance is expected to increase due to inherent variability among in vivo measurements; thus, the performance reported here represents a lower bound. For the TAEUS device, the single-operator repeated-measurement standard deviation was computed within participants with multiple valid scans and then averaged across participants. The resulting Deming regression confidence interval was compared with the identity line (MRI-PDFF = TAFF) to assess method equivalence.
In addition, the accuracy of TAEUS to differentiate grades of steatotic liver disease was evaluated using paired MRI-PDFF measurements to estimate sensitivity, specificity, and negative and positive predictive values for binary classification. As there are no widely accepted cut-offs for MASLD disease staging other than S0-S1, cut-offs were selected based on the published studies comparing biopsy staging of SLD to MRI-PDFF measurements, with multiple cutoffs presented based on different publications [76–80]. The steatosis grade cutoffs analyzed are: S0-S1 = 5% LFF, S1-S2 = 12% & 17% LLF, and S2-S3 = 20% & 22% LFF. Additionally, the accuracy of TAEUS in determining whether a study participant has ≤8% MRI-PDFF was estimated, as clinical guidelines [81] suggest this MRI-PDFF threshold as one of the decision criteria for therapeutic intervention with Resmetirom. receiver operating characteristic (ROC) analysis was also performed at all thresholds using Harrell's C-statistic [82].
Finally, an exploratory analysis was conducted to identify demographic characteristics commonly associated with MASLD that might contribute to measurement error. To determine anatomical and population-based systematic errors, the correlation between measurement error and gender, BMI, and hip-to-waist ratio was assessed.

Results

Study subjects

Forty-nine (49) study participants consented, enrolled, and were scanned, with eight (8) excluded due to the exclusion criteria shown in Table 1. A preliminary U/S scan determined that three subjects had subcutaneous fat thickness of less than 6 mm. Due to anatomical variation, the liver could not be identified in three excluded study participants who lacked the required right intercostal ultrasound access. Two subjects were excluded due to the presence of perihepatic fat

at the measurement site, which was later confirmed by MRI in each case. Finally, one additional subject could not be analyzed due to MRI-PDFF motion artifacts, preventing accurate measurement of LFF.

The study population is described in Table 2 below. The study population had a higher mean BMI than the US general population, as only subjects with suspected elevated liver fat were enrolled. The mean BMI of study participants was 34 kg/m² in females and 32.2 kg/m² in males, compared with the national average of 29.6 kg/m² [83]. Two-thirds of the study participants are obese (BMI > 30). Waist circumference was also larger than the national average and exceeded the threshold for abdominal obesity. For females, the mean waist circumference was 113 cm, substantially exceeding the national average of 95.5 cm and the cutoff for abdominal obesity of 88 cm. For males, the mean waist circumference was over 112 cm, exceeding the national average of 100.5 cm and the cutoff for abdominal obesity of 102 cm [83].

Table 2 - Demographics and Body Habitus of Study Participants

Gender	N Obs	Variable	Units	Mean	Std Dev	Minimum	Maximum
Female	25	Age	years	54.2	12.0	34.0	74.0
		Height	cm	165.7	7.6	153.0	184.0
		Weight	kg	93.6	22.0	54.0	148.8
		BMI	kg/m^2	34.0	7.1	21.0	47.0
		Hip circumference	cm	120.3	16.7	84.0	150.0
		Waist circumference	cm	113.4	16.8	77.0	148.0
		Waist to hip ratio	#	0.95	0.09	0.79	1.17
Male	15	Age	years	49.2	10.3	29.0	65.0
		Height	cm	176.5	8.0	157.0	186.0
		Weight	kg	100.5	14.3	79.2	130.0
		BMI	kg/m^2	32.2	3.7	24.8	37.6
		Hip circumference	cm	112.0	6.1	103.0	123.0
		Waist circumference	cm	112.1	13.8	83.0	134.0
		Waist to hip ratio	#	1.01	0.09	0.81	1.13
Both	40	Age	years	52.3	11.5	29.0	74.0
		Height	cm	169.8	9.3	153.0	186.0
		Weight	kg	96.2	19.6	54.0	148.8
		BMI	kg/m^2	33.3	6.0	21.0	47.0
		Hip circumference	cm	117.1	14.2	84.0	150.0
		Waist circumference	cm	112.9	15	77.0	148.0
		Waist to hip ratio	#	0.97	0.09	0.79	1.17

Due to enrollment criteria, the incidence of MASLD in this study was higher than that of the US population [15]. The distribution of liver steatosis grades is shown in Figure 3(A). This more

uniform distribution of MASLD grades enabled adequate estimation of TAEUS performance across all MASLD grades. Similarly, the distributions of body habitus (subcutaneous fat thickness and liver capsule depth) shown in Figures 3(B) and 3(C), respectively, indicate a greater tendency toward a larger body habitus.

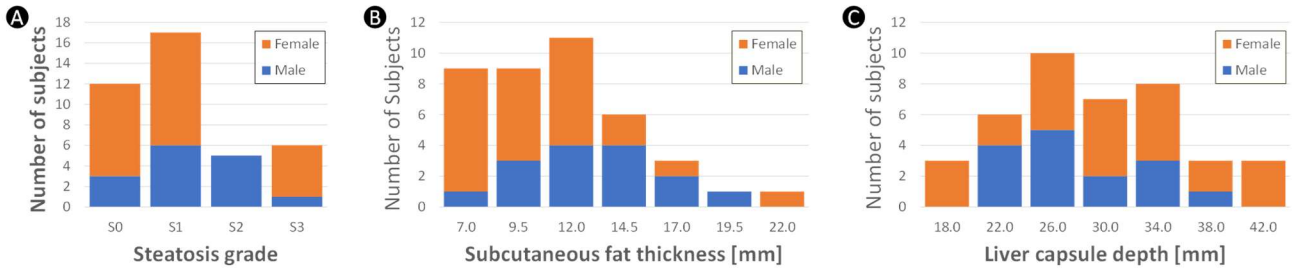

Figure 3 -Study population characteristics by gender: (A) Steatosis grade (by MRI-PDFF) of the study participants, (B) Subcutaneous fat thickness (by U/S), (C) Liver capsule depth (by U/S)

TAFF performance

The mean estimated TAFF value and the paired MRI-PDFF measurement were used to generate a Bland-Altman plot to visualize the distribution of error across MASLD grades. The mean TAFF measurement error for the 40 study participants who met the inclusion criteria was 1.95% LFF. This 1.95% error was subtracted from each study participant's TAFF value to correct for bias. Figure 4A shows that across a wide range of LFF (1%-32%), and for all steatosis grades (colored differently), the average absolute error is 3.04%. TAFF measurement error was higher in study participants with low MRI-PDFF values than in those with higher LFF. The limits of agreement (LOA) were ±7.21% LFF. Figure 4B illustrates the distribution of absolute error across LFF. It represents the percentage of subjects whose measurement error falls below a given threshold. The percentiles were calculated using linear interpolation of the empirical cumulative distribution function (folded CDF). From the plot, we observe that 49.1% of study participants had a TAFF estimate within 2.5% of their MRI-PDFF value, and 89.1% within 5.0%. These plots illustrate the accuracy and consistency of the TAFF estimates of LFF across the study population compared with MRI-PDFF measurements.

The within-subject variability of TAFF was assessed, yielding an average standard deviation of 2.66% (variance of 7.085) LFF for repeated measurements with TAEUS for subjects with more than a single valid scan. Deming regression, accounting for TAFF's higher variability relative to MRI-PDFF (variance 2.778, yielding a TAFF to MRI-PDFF variance ratio of 2.55), was used to evaluate agreement between TAFF and MRI-PDFF estimates of LFF, as shown in Figure 4B. The Deming regression yielded a slope of 0.86 (95% confidence interval: 0.71 to 1.02) and an intercept of 1.31% LFF (95% confidence interval: -0.30 to 2.93), which includes the identity line, indicating

good agreement between TAEUS and MRI-PDFF. In addition, the Pearson correlation coefficient was determined to be 0.89, further demonstrating a strong correlation between TAFF and MRI-PDFF measurements of LFF. The variability of repeated TAFF estimates within subjects was higher at low LFF than at higher LFF.

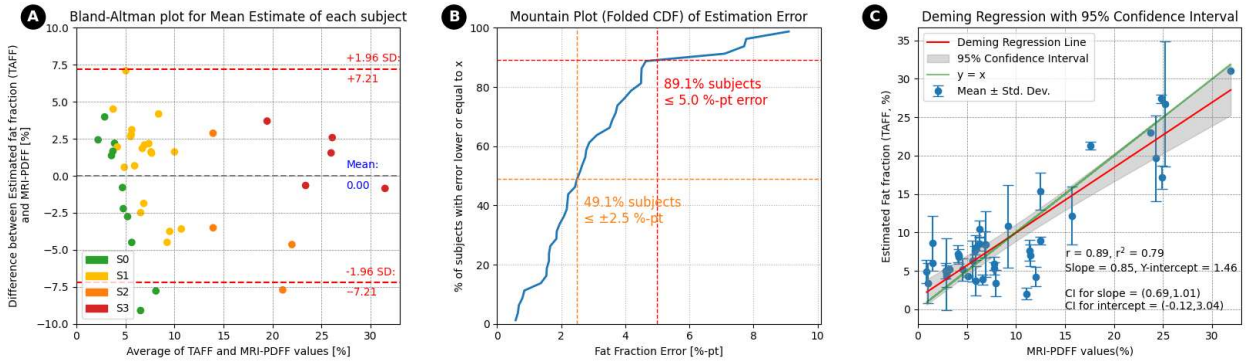

Figure 4 -Analysis of study results in comparison to MRI-PDFF. (A) Bland-Altman plot of the estimation error (in % fat fraction) as a function of the averaged fat fraction. (B) Error distribution plot (C) Deming regression plot

The classification accuracy of TAFF across different LFF thresholds is summarized in Table 3 below. Consistent with the earlier observation that signal variability is higher at low fat fractions, classification performance is limited at the lowest LFF threshold (5%). As LFF increases, both sensitivity and specificity improve, resulting in higher overall accuracy and a larger AUROC. The positive predictive values are good across the board, and the negative predictive values increase markedly at moderate fat fractions. Furthermore, as illustrated in Figure 5, the ROC curves show a marked improvement at higher fat fraction thresholds, accompanied by corresponding increases in AUROC, reflecting enhanced classification performance of TAFF for moderate-to-severe liver fat.

Table 3 - Binary classification results with various threshold values

Threshold Fat Fraction	5% LFF (S0-S1)	8% LFF (THrβ)	12% LFF (S1-S2)	17% LFF (S1-S2)	20% LFF (S2-S3)	22% LFF (S2-S3)
PPV (%)	75.9	68.8	100.0	100.0	80.0	100.0
NPV (%)	45.5	83.3	93.6	100.0	94.3	94.4
Sensitivity (%)	78.6	73.3	81.8	100.0	66.7	66.7
Specificity (%)	41.7	80.0	100.0	100.0	97.1	100.0
Accuracy (%)	67.5	77.5	95.0	100.0	92.5	95.0
AUROC	0.74	0.83	0.92	1.0	0.99	0.99

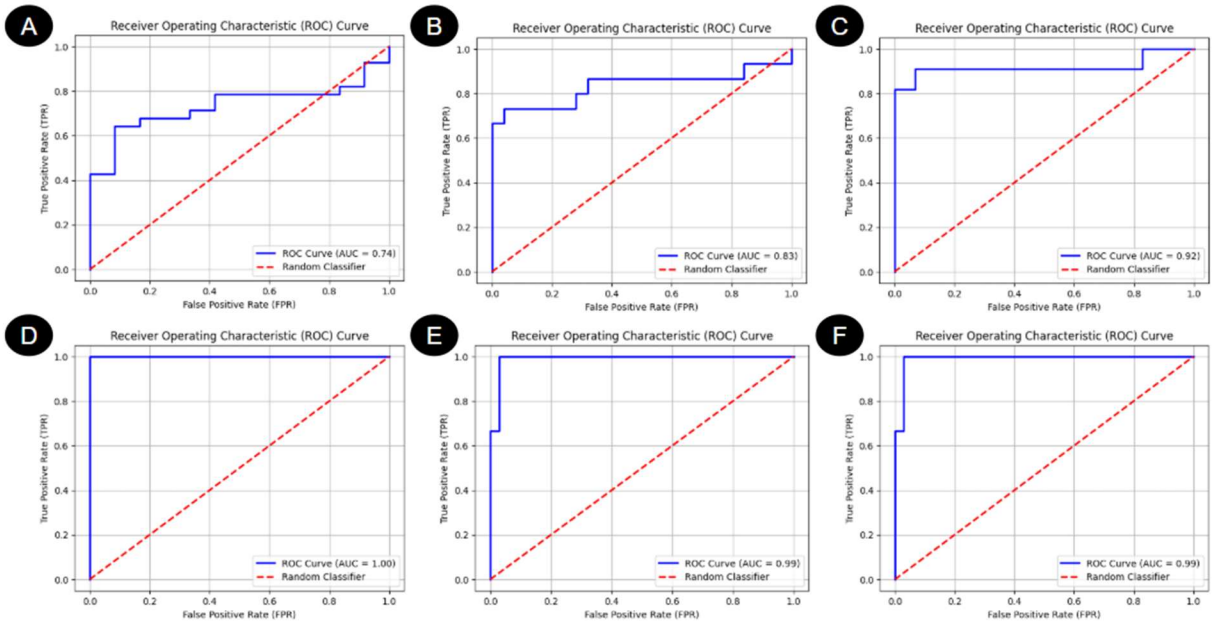

Figure 5 -ROC curves for the binary classification results (A) Threshold = 5% (B) Threshold = 8% (C) Threshold = 12% (D) Threshold = 17% (E) Threshold = 20% (F) Threshold = 22%

Relationship between TAFF and demographic information

Differences between TAFF and MRI were analyzed with respect to demographics. We found that the average difference in males (n = 15) was 1.6% LFF lower than in females (n = 25), yielding a p-value of 0.26. This finding suggests that there is no statistically significant difference between the genders. Additionally, a statistical analysis was conducted to investigate the relationship between the various metadata collected on study participants and the estimation differences as reported in Table 4 below.

Table 4 - Relationship between meta-variables and estimation errors

Variable	Correlation	p-value
Age	-0.080	0.2574
Height	-0.158	0.3295
Weight	-0.150	0.3563
BMI	-0.056	0.7370
Hip circumference	-0.052	0.7530
Waist circumference	-0.1049	0.5252
Waist/hip ratio	-0.085	0.6114

This analysis found low correlations and no statistically significant relationships between metadata variables and TAEUS estimation errors. Figure 6 presents the distribution of TAFF

estimation errors categorized by participant demographics and anthropometric data. These box plots illustrate the median, interquartile range, and outliers for each subgroup (gender, height, weight, BMI, and body circumference metrics). Consistent with the low correlation coefficients ($r < 0.16$) and non-significant p-values ($p > 0.25$) previously noted, the plots show no systematic trends or distinct separation between categories. While specific subgroups, such as the 90 to 110 kg weight class or the 30 to 35 BMI range, exhibit greater variability, the substantial overlap in error distributions across those bins reinforces the conclusion that these metadata variables are not reliable predictors of TAFF estimation performance.

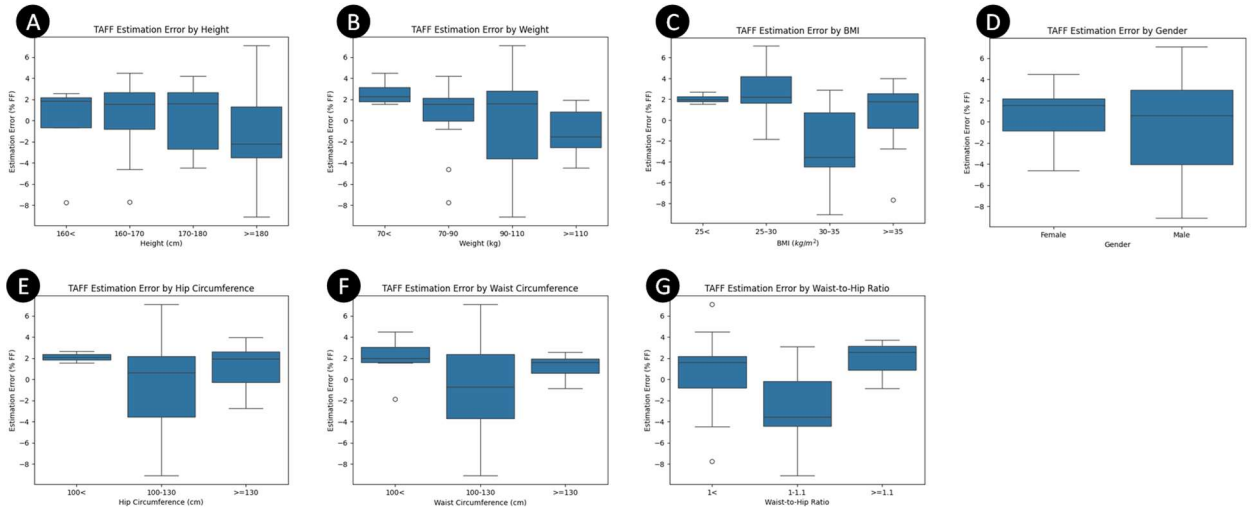

Figure 6 - Box Plots of TAFF Estimation Errors Across Demographic and Anthropometric subgroups (A) Height (B) Weight (C) BMI (D) Gender (E) Hip circumference (F) Waist circumference (G) Waist-to-Hip ratio

Discussion

This single-site feasibility study is the first of its kind to utilize thermoacoustic principles to estimate fat in human subjects. The TAEUS liver system accurately estimates liver fat across a wide range of body habitus, including mild to severe disease. The portable TAEUS liver system exhibits comparable performance to MRI-PDFF, with costs and mobility similar to those of cart-based ultrasound. Thus, it indicates the potential of such technology as a valuable tool to aid in the diagnosis of MASLD, informing therapeutic decisions, and monitoring disease progression.

Bland-Altman plots across all disease grades show the limits of agreement to be ±7.21% as compared to the reference standard MRI-PDFF. The cumulative error distribution (mountain plot) indicates that half (49.1%) of study participants had a TAFF estimate within 2.5% of their MRI-PDFF value, and the vast majority (89.1%) within 5.0%. These results are significantly better than established methods such as CAP, which exhibits a 95% limit of agreement for ±12% in fat fraction after converting its native measurements to match the MRI [84]. More importantly, the TAEUS

Liver system estimates of LFF were strongly correlated with MRI-PDFF scores (r = 0.89). In contrast, estimates of LFF with quantitative ultrasound suggest a wide disparity of results with reported correlations with baseline MRI-PDFF of 0.49-0.89 [47,85–87] for baseline MRI-PDFF and only 0.52 for changes in MRI-PDFF [85,86]. In contrast to QUS approaches, the TAEUS Liver system has a constant error and does not exhibit errors proportional to the estimated value.

In predicting the presence of moderate to severe steatosis (S2-S3) at the 12% LFF threshold, TAEUS achieves 100% specificity and PPV of 100%, with an AUROC of 0.92 in the available cohort. These results indicate exceptional accuracy in identifying study participants with moderate to severe SLD, a critical clinical threshold for urgent and aggressive management of MASLD and MASH. In contrast, large meta-analyses of widely used point-of-care quantitative U/S methods for assessing moderate steatosis report AUROCs of approximately 0.82 and much lower specificities ranging from 74% to 79% [91,92]. While these existing tools have a role in screening, their relatively low specificity often necessitates confirmatory testing. The data gathered in this study suggest that the TAEUS Liver system may overcome many of the limitations of quantitative U/S approaches, offering high diagnostic accuracy when comparable to MRI-PDFF as the reference standard (AUROC >0.90) and far exceeding the statistical performance of current methods for quantifying moderate liver fat.

Demographic analysis revealed no significant difference in errors between participants of different sexes. In addition, the TAEUS Liver system demonstrated low correlation (r<0.16) between estimation errors and patient age or body habitus parameters (e.g., height, BMI, waist circumference). This implies that the method is applicable across various body types, age groups, and sexes. These joint findings suggest that participant characteristics do not significantly explain variation in TAFF estimation errors, and incorporating these variables as additional inputs is unlikely to enhance prediction accuracy. In contrast, some quantitative ultrasound methods showed a nonlinear relationship (i.e., proportional error) with MRI-PDFF [88,89]. Some clinical reported findings show a significant dependence of LFF measurement accuracy on BMI [87,90], which was not demonstrated by the TAEUS liver system.

These overall findings support TAEUS's potential as an accurate, non-invasive, point-of-care solution that could address the cost and access constraints of MRI and the limitations of current quantitative ultrasound methods. The high PPV and NPV allow for the accurate identification of individuals with severe MASLD and for separating healthy individuals and those with mild MASLD from individuals with moderate and severe MASLD. These trends highlight that TAFF is most effective for detecting moderate to severe steatosis, whereas classification at very low fat-fractions remains more challenging due to inherently weaker signals. Specifically, at an LFF of 8%, the Resmetirom (THrβ) treatment threshold, the negative predictive value exceeds 83%, suggesting that TAEUS may be valuable in guiding therapeutic decisions and monitoring disease progression.

The current feasibility study also highlights some limitations of thermoacoustic imaging and the first-generation TAEUS system. In particular, the current system can only resolve contrast differences in tissue conductivity. Thus, it suffers from a lack of signal at low LFF as the differences between lean liver tissue and (lean) muscle become minute, leading to a lower contrast-to-noise ratio and more variable measurements. As liver tissue becomes fattier, the contrast increases, and with it, the robustness of the liver fat estimation. This limitation of the first-generation TAEUS liver thermoacoustic system can be addressed by incorporating a more sensitive transducer to improve signal resolution for low LFF. The current 16-element, 0.5 MHz phased-array configuration offers limited performance that can be improved. In addition, the improvement in contrast with increasing fat fraction, rather than extinguishing signal observed with pure ultrasonic methods [87], suggests that a combined quantitative ultrasound and TA device can deliver improved performance across all steatosis grades.

Another difficulty with this first-generation TA system is the need to rely on a separate U/S device to acquire tissue anatomy before a TA scan can proceed. Proper positioning of the wireless ultrasound probe and the larger TAEUS probe contributed greatly to inaccuracies in estimation, lengthened the session time, and placed additional strain on the user. This observation suggests that a future device combining both ultrasound and TA capabilities would be much easier to use and would enjoy greater accuracy in fat fraction estimation.

It is also worth noting that while the results reported in this study are quite promising, they are based on a preliminary study with a single site, a single user, and a limited number of patients (N = 40). A larger-scale, multi-site, multi-user follow-up study would be required to test the reproducibility and repeatability of TAEUS and to establish the performance of this novel method. Thus, it is expected that in the coming years, more studies will be conducted using TAEUS, opening new avenues for accurate, low-cost, portable liver fat estimation and monitoring.

Acknowledgments

The authors express their gratitude to Chris Davis, PhD, for his review and meaningful improvements to this manuscript, and to Professor Emeritus Gary Cutter for his statistical review of the data analysis. We also thank Professor Thomas L. Chenevert of the Department of Radiology at the University of Michigan for his technical assistance in acquiring MRI-PDFF measurements. Finally, we acknowledge Ms. Ava Ohlgren for her invaluable support in recruiting, scheduling, and accompanying the study subjects.

References

1. Koo DJ, Lee WY. The crosstalk between insulin resistance and nonalcoholic fatty liver disease/metabolic dysfunction-associated fatty liver disease: a culprit or a consequence? *Cardiovasc Prev Pharmacother*. 2022;4(4):132-141. doi:10.36011/cpp.2022.4.e17

2. Vesković M, Šutulović N, Hrnčić D, Stanojlović O, Macut D, Mladenović D. The interconnection between hepatic insulin resistance and metabolic dysfunction-associated steatotic liver disease-the transition from an adipocentric to liver-centric approach. *Curr Issues Mol Biol*. 2023;45(11):9084-9102. doi:10.3390/cimb45110570

3. Diehl AM. Tumor necrosis factor and its potential role in insulin resistance and nonalcoholic fatty liver disease. *Clin Liver Dis*. 2004;8(3):619-638, x. doi:10.1016/j.cld.2004.04.012

4. Meex RCR, Watt MJ. Hepatokines: linking nonalcoholic fatty liver disease and insulin resistance. *Nat Rev Endocrinol*. 2017;13(9):509-520. doi:10.1038/nrendo.2017.56

5. Stefan N, Schick F, Birkenfeld AL, Häring HU, White MF. The role of hepatokines in NAFLD. *Cell Metab*. 2023;35(2):236-252. doi:10.1016/j.cmet.2023.01.006

6. Zhao YC, Zhao GJ, Chen Z, She ZG, Cai J, Li H. Nonalcoholic fatty liver disease. *Hypertension*. 2020;75(2):275-284. doi:10.1161/hypertensionaha.119.13419

7. Miao X, Alidadipour A, Saed V, et al. Hepatokines: unveiling the molecular and cellular mechanisms connecting hepatic tissue to insulin resistance and inflammation. *Acta Diabetol*. 2024;61(11):1339-1361. doi:10.1007/s00592-024-02335-9

8. Alam S, Mustafa G, Alam M, Ahmad N. Insulin resistance in development and progression of nonalcoholic fatty liver disease. *World J Gastrointest Pathophysiol*. 2016;7(2):211-217. doi:10.4291/wjgp.v7.i2.211

9. Masarone M, Rosato V, Dallio M, et al. Role of oxidative stress in pathophysiology of nonalcoholic fatty liver disease. *Oxid Med Cell Longev*. 2018;2018(1):1-14. doi:10.1155/2018/9547613

10. Gonzalez A, Huerta-Salgado C, Orozco-Aguilar J, et al. Role of oxidative stress in hepatic and extrahepatic dysfunctions during nonalcoholic fatty liver disease (NAFLD). *Oxid Med Cell Longev*. 2020;2020:1617805. doi:10.1155/2020/1617805

11. Petrescu M, Vlaicu SI, Ciumărnean L, et al. Chronic inflammation-A link between nonalcoholic fatty liver disease (NAFLD) and dysfunctional adipose tissue. *Medicina (Kaunas)*. 2022;58(5):641. doi:10.3390/medicina58050641

12. Targher G, Byrne C, Tilg H. NAFLD and increased risk of cardiovascular disease: clinical associations, pathophysiological mechanisms and pharmacological implications. *Gut*. 2020;69:1691-1705. doi:10.1136/gutjnl-2020-320622

13. Mantovani A, Morieri ML, Aldigeri R, et al. MASLD, hepatic steatosis and fibrosis are associated with the prevalence of chronic kidney disease and retinopathy in adults with type 1 diabetes mellitus. *Diabetes Metab*. 2024;50(1):101497. doi:10.1016/j.diabet.2023.101497

14. Mikkelsen ACD, Kjærgaard K, Schapira AHV, Mookerjee RP, Thomsen KL. The liver-brain axis in metabolic dysfunction-associated steatotic liver disease. *Lancet Gastroenterol Hepatol*. 2025;10(3):248-258. doi:10.1016/S2468-1253(24)00320-0

15. Riazi K, Azhari H, Charette JH, et al. The prevalence and incidence of NAFLD worldwide: a systematic review and meta-analysis. *Lancet Gastroenterol Hepatol*. 2022;7(9):851-861. doi:10.1016/S2468-1253(22)00165-0

16. C. CPC. 4. Comprehensive Medical Evaluation and Assessment of Comorbidities: Standards of Care in Diabetes—2025. *Diabetes Care*. 2025;48(1):S59-S85. https://sentucuman.com.ar/docs/4ADA2025.pdf

17. Younossi ZM, Koenig AB, Abdelatif D, Fazel Y, Henry L, Wymer M. Global epidemiology of nonalcoholic fatty liver disease-Meta-analytic assessment of prevalence, incidence, and outcomes. *Hepatology*. 2016;64(1):73-84. doi:10.1002/hep.28431

18. Le MH, Yeo YH, Li X, et al. 2019 global NAFLD prevalence: A systematic review and meta-analysis. *Clin Gastroenterol Hepatol*. 2022;20(12):2809-2817.e28. doi:10.1016/j.cgh.2021.12.002

19. Paik JM. Clinical burden of nonalcoholic fatty liver disease in the United States: 2016-2025. *Hepatology*. Published online 2020:2016-2025.

20. Younossi Z. Nonalcoholic steatohepatitis (NASH): A review of the natural history, current challenges, and new therapeutic options. *Journal of Hepatology*. Published online 2019.

21. Mahathi BI, Srikanth R. Non-Alcoholic Fatty Liver Disease: An Emerging Cardiovascular Risk Enhancer. Published online 2022.

22. Oh YH, Jeong S, Park SJ, Ahn JC, Park SM. Reversal of nonalcoholic fatty liver disease reduces the risk of cardiovascular disease among Korean. *Medicine (Baltimore)*. 2023;102(44):e35804. doi:10.1097/MD.0000000000035804

23. Tsamos G, Vasdeki D, Koufakis T, Michou V, Makedou K, Tzimagiorgis G. Therapeutic potentials of reducing liver fat in non-alcoholic fatty liver disease: Close association with type 2 diabetes. *Metabolites*. 2023;13(4):517. doi:10.3390/metabo13040517

24. Laursen TL, Hagemann CA, Wei C, et al. Bariatric surgery in patients with non-alcoholic fatty liver disease - from pathophysiology to clinical effects. *World J Hepatol*. 2019;11(2):138-149. doi:10.4254/wjh.v11.i2.138

25. Biobaku F, Ghanim H, Monte SV, Caruana JA, Dandona P. Bariatric surgery: Remission of inflammation, cardiometabolic benefits, and common adverse effects. *J Endocr Soc*. 2020;4(9):bvaa049. doi:10.1210/jendso/bvaa049

26. Vilar-Gomez E, Martinez-Perez Y, Calzadilla-Bertot L, et al. Weight loss through lifestyle modification significantly reduces features of nonalcoholic steatohepatitis. *Gastroenterology*. 2015;149(2):367-378.e5; quiz e14-e15. doi:10.1053/j.gastro.2015.04.005

27. Kotsiliti E. Drug approvals in gastroenterology and hepatology in 2024. *Nature reviews Gastroenterology & hepatology*. Published online January 13, 2025. doi:10.1038/s41575-025-

01036-0

28. Sanyal AJ, Newsome PN, Kliers I, et al. Phase 3 trial of semaglutide in metabolic dysfunction-associated steatohepatitis. *New England Journal of Medicine*. 2025;392(21):2089-2099. https://scholarindexing.com/uploads/files/8pu3_1ome6lcxkb.pdf

29. McEwan P, Bøg M, Faurby M, et al. EE497 the cost-effectiveness of semaglutide 2.4MG in patients with overweight/obesity and cardiovascular disease from the select trial. *Value Health*. 2024;27(6):S148. doi:10.1016/j.jval.2024.03.2261

30. Bacha Z, Javed J, Sheraz M, et al. Efficacy and safety of semaglutide on cardiovascular outcomes in patients with type 2 diabetes: A systematic review and meta-analysis of randomized controlled trials. *Cardiol Rev*. Published online September 19, 2025. doi:10.1097/CRD.0000000000001057

31. Kishimori T, Kato T, Wada A, et al. Cardiovascular outcomes and safety of semaglutide in non-overweight populations with type 2 diabetes: A comparison with dipeptidyl peptidase 4 inhibitors. *Eur Heart J Qual Care Clin Outcomes*. 2025;(qcaf065). doi:10.1093/ehjqcco/qcaf065

32. Sumida Y, Nakajima A, Itoh Y. Limitations of liver biopsy and non-invasive diagnostic tests for the diagnosis of nonalcoholic fatty liver disease/nonalcoholic steatohepatitis. *World J Gastroenterol*. 2014;20(2):475-485. doi:10.3748/wjg.v20.i2.475

33. Heyens LJM, Busschots D, Koek GH, Robaeys G, Francque S. Liver fibrosis in non-alcoholic fatty liver disease: From liver biopsy to non-invasive biomarkers in diagnosis and treatment. *Front Med (Lausanne)*. 2021;8:615978. doi:10.3389/fmed.2021.615978

34. Caussy C, Reeder SB, Sirlin CB, Loomba R. Noninvasive, quantitative assessment of liver fat by MRI-PDFF as an endpoint in NASH trials. *Hepatology*. 2018;68(2):763-772. doi:10.1002/hep.29797

35. Zhang YX, Feng YP, You CL, Zhang LY. The diagnostic value of MRI-PDFF in hepatic steatosis of patients with metabolic dysfunction-associated steatotic liver disease: a systematic review and meta-analysis. *BMC Gastroenterol*. 2025;25(1):451. doi:10.1186/s12876-025-04017-4

36. Mikolasevic I, Orlic L, Franjic N, Hauser G, Stimac D, Milic S. Transient elastography (FibroScan(®)) with controlled attenuation parameter in the assessment of liver steatosis and fibrosis in patients with nonalcoholic fatty liver disease - Where do we stand? *World J Gastroenterol*. 2016;22(32):7236-7251. doi:10.3748/wjg.v22.i32.7236

37. Malandris K, Korakas E, Sarakapina A, et al. Accuracy of controlled attenuation parameter for liver steatosis in high-risk patients for MASLD using MRI-proton density fat fraction as reference standard. *Dig Dis Sci*. 2025;70(2):814-824. doi:10.1007/s10620-024-08799-7

38. Martinou E, Pericleous M, Stefanova I, Kaur V, Angelidi AM. Diagnostic modalities of non-Alcoholic Fatty Liver Disease: From biochemical biomarkers to multi-omics non-invasive approaches. *Diagnostics (Basel)*. 2022;12(2):407. doi:10.3390/diagnostics12020407

39. Lauschke VM. Practice guidance documents for the diagnosis and management of non-alcoholic fatty liver disease-recent updates and open questions. *Hepatobiliary Surg Nutr*. 2023;12(5):780-784. doi:10.21037/hbsn-23-376

40. Wear KA, Han A, Rubin JM, et al. US backscatter for liver fat quantification: An AIUM-RSNA QIBA pulse-echo quantitative Ultrasound initiative. *Radiology*. 2022;305(3):526-537. doi:10.1148/radiol.220606

41. Park J, Lee JM, Lee G, Jeon SK, Joo I. Quantitative evaluation of hepatic steatosis using advanced imaging techniques: Focusing on new quantitative ultrasound techniques. *Korean J Radiol*. 2022;23(1):13-29. doi:10.3348/kjr.2021.0112

42. Han A. US attenuation coefficient for liver fat quantification: A need for standardization. *Radiology*. 2024;313(1):e242511. doi:10.1148/radiol.242511

43. Adamson C, Dong J, Hagenstein LD, Jenkins J, Lee M, Gao J. The effect of measurement depth and technical considerations in performing liver attenuation imaging. *J Transl Gastroenterol*. 2024;2(1):1-8. doi:10.14218/jtg.2023.00047

44. Ferraioli G, Raimondi A, Maiocchi L, et al. Liver fat quantification with ultrasound: Depth dependence of attenuation coefficient: Depth dependence of attenuation coefficient. *J Ultrasound Med*. 2023;42(10):2247-2255. doi:10.1002/jum.16242

45. Jin H, Jiao M, Yu C, et al. Discovery of ultrasound-derived fat fraction as a non-invasive tool for MASLD diagnosis. *Eur J Med Res*. 2025;30(1):1014. doi:10.1186/s40001-025-03229-4

46. Xue L, Zhu Y, Cheng G, et al. Ultrasound-derived fat fraction for the noninvasive quantification of hepatic steatosis: a prospective multicenter study. *Insights Imaging*. 2025;16(1):237. doi:10.1186/s13244-025-02092-5

47. Gao R, Han J, Song D, et al. Quantitative assessment of hepatic steatosis by ultrasound-guided attenuation parameter in patients with impaired glucose tolerance. *Insights Imaging*. 2025;16(1):247. doi:10.1186/s13244-025-02123-1

48. Factors associated with obtaining lower IQR-CAP values in the detection of hepatic steatosis by transient elastography. *Annals of Hepatology*. 2025;30(1):101762. doi:10.1016/j.aohep.2024.101762

49. Heinitz S, Müller J, Jenderka KV, et al. The application of high-performance ultrasound probes increases anatomic depiction in obese patients. *Sci Rep*. 2023;13(1):16297. doi:10.1038/s41598-023-43509-9

50. Maar M, Lee J, Tardi A, Zheng YY, Wong C, Gao J. Inter-transducer variability of ultrasound image quality in obese adults: Qualitative and quantitative comparisons. *Clin Imaging*. 2022;92:63-71. doi:10.1016/j.clinimag.2022.09.010

51. Bril F, Ortiz-Lopez C, Lomonaco R, et al. Clinical value of liver ultrasound for the diagnosis of nonalcoholic fatty liver disease in overweight and obese patients. *Liver Int*. 2015;35(9):2139-2146. doi:10.1111/liv.12840

52. Johansen S, Åberg F, Tsochatzis EA, Krag A. Screening for advanced steatotic liver disease. *Lancet Gastroenterol Hepatol*. 2025;10(9):842-854. doi:10.1016/S2468-1253(25)00097-4

53. Yang Y, Xia Z, Xia H, Li Y, Liu G, Xu J. Applied current thermoacoustic imaging for biological tissues.

Technol Health Care. 2020;28(S1):57-65. doi:10.3233/THC-209007

54. Gabriel S, Lau RW, Gabriel C. The dielectric properties of biological tissues: III. Parametric models for the dielectric spectrum of tissues. *Phys Med Biol*. 1996;41(11):2271-2293. doi:10.1088/0031-9155/41/11/003

55. Gabriel S, Lau RW, Gabriel C. The dielectric properties of biological tissues: II. Measurements in the frequency range 10 Hz to 20 GHz. *Phys Med Biol*. 1996;41(11):2251-2269. doi:10.1088/0031-9155/41/11/002

56. Gabriel C, Gabriel S, Corthout E. The dielectric properties of biological tissues: I. Literature survey. *Phys Med Biol*. 1996;41(11):2231-2249. doi:10.1088/0031-9155/41/11/001

57. Ku G, Wang LV. Scanning microwave-induced thermoacoustic tomography: signal, resolution, and contrast. *Med Phys*. 2001;28(1):4-10. doi:10.1118/1.1333409

58. Wang X, Huang L, Chi Z, Jiang H. Integrated thermoacoustic and ultrasound imaging based on the combination of a hollow concave transducer array and a linear transducer array. *Phys Med Biol*. 2021;66(11):115011. doi:10.1088/1361-6560/abfc91

59. Roggenbuck MA, Walker RD, Catenacci JW, Patch SK. Volumetric thermoacoustic imaging over large fields of view. *Ultrason Imaging*. 2013;35(1):57-67. doi:10.1177/0161734612471664

60. Razansky D, Kellnberger S, Ntziachristos V. Near-field radiofrequency thermoacoustic tomography with impulse excitation: NRT. *Med Phys*. 2010;37(9):4602-4607. doi:10.1118/1.3467756

61. Liu Q, Liang X, Qi W, Gong Y, Jiang H, Xi L. Biomedical microwave-induced thermoacoustic imaging. *J Innov Opt Health Sci*. 2022;15(04). doi:10.1142/s1793545822300075

62. Li J, Wu Z, Peng C, Song L, Luo Y. Microwave-induced thermoacoustic imaging for the early detection of canine intracerebral hemorrhage. *Front Physiol*. 2022;13:1067948. doi:10.3389/fphys.2022.1067948

63. Islam T, Avanaki K. Thermoacoustic imaging: Principles and applications in preclinical research. In: *Biomaterials, Bioengineering and Sustainability*. Springer Nature Switzerland; 2025:365-397. doi:10.1007/978-3-031-99410-4_19

64. Song L, Peng W, Lu Q, et al. Thermoacoustic imaging using single-channel data acquisition system for non-invasive assessment of liver microwave ablation: A feasibility study. *Photonics*. 2024;11(9):807. doi:10.3390/photonics11090807

65. Kruger RA, Kopecky KK, Aisen AM, Reinecke DR, Kruger GA, Kiser WL Jr. Thermoacoustic CT with radio waves: a medical imaging paradigm. *Radiology*. 1999;211(1):275-278. doi:10.1148/radiology.211.1.r99ap05275

66. Dixit N, Stang PP, Pauly JM, Scott GC. Thermo-acoustic ultrasound for detection of RF-induced device lead heating in MRI. *IEEE Trans Med Imaging*. 2018;37(2):536-546. doi:10.1109/TMI.2017.2764425

67. Thronton M. *Thermoacoustic Imaging: A Novel Method for Quantifying Fat in NAFLD*. Endra Life

Sciences, Inc; 2018. irp.cdn-website.com/c88af476/files/uploaded/Endra_WhitePaper_WhyItWorks.pdf

68. International Electrotechnical Commission. *IEC 60601-2-33; Medical Electrical Equipment*.; 2023.

69. Institute of Electrical and Electronics Engineers (IEEE). *IEEE C95.1-2019; Standard for Safety Levels with Respect to Human Exposure to Electric, Magnetic, and Electromagnetic Fields, 0 Hz to 300 GHz*.; 2019.

70. Xu M, Wang LV. Universal back-projection algorithm for photoacoustic computed tomography. *Phys Rev E Stat Nonlin Soft Matter Phys*. 2005;71(1 Pt 2):016706. doi:10.1103/PhysRevE.71.016706

71. Bonekamp S, Tang A, Mashhood A, et al. Spatial distribution of MRI-Determined hepatic proton density fat fraction in adults with nonalcoholic fatty liver disease: Spatial Distribution of Liver Fat in NAFLD. *J Magn Reson Imaging*. 2014;39(6):1525-1532. doi:10.1002/jmri.24321

72. Martin Bland J, Altman D. Statistical methods for assessing agreement between two methods of clinical measurement. *Lancet*. 1986;327(8476):307-310. doi:10.1016/s0140-6736(86)90837-8

73. Deming WE. Statistical adjustment of data. *pp*. 1943;261. https://psycnet.apa.org/record/1944-00642-000

74. Guidance D. Guidance for Industry. https://pink.citeline.com/-/media/supporting-documents/pink-sheet/2022/12/p1222fda_2.pdf

75. Gassert FT, Kufner A, Gassert FG, et al. MR-based proton density fat fraction (PDFF) of the vertebral bone marrow differentiates between patients with and without osteoporotic vertebral fractures. *Osteoporos Int*. 2022;33(2):487-496. doi:10.1007/s00198-021-06147-3

76. Tang A, Tan J, Sun M, et al. Nonalcoholic fatty liver disease: MR imaging of liver proton density fat fraction to assess hepatic steatosis. *Radiology*. 2013;267(2):422-431. doi:10.1148/radiol.12120896

77. Park S, Kwon JH, Kim SY, et al. Cutoff values for diagnosing hepatic steatosis using contemporary MRI-proton density fat fraction measuring methods. *Korean J Radiol*. 2022;23(12):1260-1268. doi:10.3348/kjr.2022.0334

78. Kühn JP, Hernando D, Muñoz del Rio A, et al. Effect of multipeak spectral modeling of fat for liver iron and fat quantification: correlation of biopsy with MR imaging results. *Radiology*. 2012;265(1):133-142. doi:10.1148/radiol.12112520

79. Szczepaniak LS, Nurenberg P, Leonard D, et al. Magnetic resonance spectroscopy to measure hepatic triglyceride content: prevalence of hepatic steatosis in the general population. *Am J Physiol Endocrinol Metab*. 2005;288(2):E462-E468. doi:10.1152/ajpendo.00064.2004

80. Tang A, Desai A, Hamilton G, et al. Accuracy of MR imaging-estimated proton density fat fraction for classification of dichotomized histologic steatosis grades in nonalcoholic fatty liver disease. *Radiology*. 2015;274(2):416-425. doi:10.1148/radiol.14140754

81. Chen VL, Morgan TR, Rotman Y, et al. Erratum: Resmetirom therapy for metabolic dysfunction-associated steatotic liver disease: October 2024 updates to AASLD Practice Guidance. *Hepatology*.

Published online February 12, 2025. doi:10.1097/HEP.0000000000001186

82. Harrell FE Jr, Califf RM, Pryor DB, Lee KL, Rosati RA. Evaluating the yield of medical tests. *JAMA*. 1982;247(18):2543-2546. doi:10.1001/jama.1982.03320430047030

83. Sun JY, Huang WJ, Hua Y, et al. Trends in general and abdominal obesity in US adults: Evidence from the National Health and Nutrition Examination Survey (2001-2018). *Front Public Health*. 2022;10:925293. doi:10.3389/fpubh.2022.925293

84. Han A, Zhang YN, Boehringer AS, et al. Assessment of hepatic steatosis in nonalcoholic fatty liver disease by using quantitative US. *Radiology*. 2020;295(1):106-113. doi:10.1148/radiol.2020191152

85. Shao CX, Ye J, Dong Z, et al. Steatosis grading consistency between controlled attenuation parameter and MRI-PDFF in monitoring metabolic associated fatty liver disease. *Ther Adv Chronic Dis*. 2021;12:20406223211033119. doi:10.1177/20406223211033119

86. Zhou Y, Nie M, Zhou H, et al. Head-to-head comparison of three different US-based quantitative parameters for hepatic steatosis assessment: a prospective study. *Abdom Radiol (NY)*. 2024;49(7):2262-2271. doi:10.1007/s00261-024-04347-z

87. De Robertis R, Spoto F, Autelitano D, et al. Ultrasound-derived fat fraction for detection of hepatic steatosis and quantification of liver fat content. *Radiol Med*. 2023;128(10):1174-1180. doi:10.1007/s11547-023-01693-8

88. Lin SC, Heba E, Wolfson T, et al. Noninvasive diagnosis of nonalcoholic fatty liver disease and quantification of liver fat using a new quantitative ultrasound technique. *Clin Gastroenterol Hepatol*. 2015;13(7):1337-1345.e6. doi:10.1016/j.cgh.2014.11.027

89. Dillman JR, Thapaliya S, Tkach JA, Trout AT. Quantification of hepatic steatosis by ultrasound: Prospective comparison with MRI proton density fat fraction as reference standard. *AJR Am J Roentgenol*. 2022;219(5):784-791. doi:10.2214/AJR.22.27878

90. Miura D. Compatibility and bias between ultrasound-guided attenuation parameter and controlled attenuation parameter for ultrasound-based hepatic steatosis assessment. *medRxiv*. Published online June 3, 2025. doi:10.1101/2025.06.03.25328166

91. Cao YT, Xiang LL, Qi F, Zhang YJ, Chen Y, Zhou XQ. Accuracy of controlled attenuation parameter (CAP) and liver stiffness measurement (LSM) for assessing steatosis and fibrosis in non-alcoholic fatty liver disease: A systematic review and meta-analysis. *EClinicalMedicine*. 2022;51(101547):101547. doi:10.1016/j.eclinm.2022.101547

92. Karlas T, Petroff D, Sasso M, et al. Individual patient data meta-analysis of controlled attenuation parameter (CAP) technology for assessing steatosis. *J Hepatol*. 2017;66(5):1022-1030. doi:10.1016/j.jhep.2016.12.022

Appendix A - Detailed description of TAFF estimation

The thermoacoustic signal generated from a tissue can be modeled as follows:

$$(Thermoacoustic\ signal\ of\ a\ tissue) \propto \Gamma\sigma E^2, \quad (1)$$

Where Γ and σ are the Gruneisen parameter and the conductivity of a given tissue, respectively, and E is the electric field strength for the tissue. Both tissue properties and electric field strengths depend on spatial location. For simplicity, the dependency on the location will be omitted.

The TAEUS probe has a limited field-of-view angle and a narrow-band ultrasound transducer. As a result, the TAEUS system is only sensitive to changes in tissue properties and to signals generated at tissue boundaries. The thermoacoustic signal at a tissue boundary can be modeled as a difference between signals generated at each tissue:

$$(Thermoacoustic\ signal\ at\ a\ tissue\ boundary) \propto (\Gamma_1\sigma_1 E_1^2 - \Gamma_2\sigma_2 E_2^2), \quad (2)$$

Where subscripts 1 and 2 denote tissues on each side of the boundary.

To estimate the fat fraction of the liver of a subject, we need to collect a signal from the boundary between the liver and a different tissue. We position the TAEUS probe on the subject's body so that the field of view includes a tissue boundary between the muscle and liver layers. The signal at this boundary can be modeled based on equation (2) as follows:

$$(Signal\ at\ the\ muscle - to - liver\ boundary) = \alpha(\Gamma_m\sigma_m E_m^2 - \Gamma_l\sigma_l E_l^2), \quad (3)$$

where α is a system-dependent coefficient and subscripts "m" and "l" denote muscle and liver, respectively. Since the electric field within the body cannot be measured, it must be estimated. Using Ansys, we modeled various body habitus with varying degrees of liver fat to estimate the electric field strength distribution of a given subject. To compensate for simplified modeling and various assumptions made, we also considered a natural reference point within the body. Instead of estimating liver fat using the above equation, another boundary based on known tissue properties was considered. The subcutaneous fat-to-muscle boundary always exists in the selected field of view containing the muscle-to-liver boundary. Since the tissue properties of both subcutaneous fat and muscle are known, the signal at this boundary can be used for calibration. We consider the ratio of signals from these boundaries as follows:

$$\frac{(Signal\ at\ the\ muscle - to - liver\ boundary)}{(Signal\ at\ the\ subcutaneous\ fat - to - muscle\ boundary)} = \frac{\Gamma_m \sigma_m E_m^2 - \Gamma_l \sigma_l E_l^2}{\Gamma_f \sigma_f E_f^2 - \Gamma_m \sigma_m E_{m^*}^2}, \quad (4)$$

where subscript f denotes subcutaneous fat, and electric field strengths E_m and E_m* are muscles adjacent to the liver and to the subcutaneous fat, respectively. The left side of the equation is from the measurements, and the right side is from the theory and the simulation. The left side of the equation is obtained by measuring the signal strengths of both boundaries. Acquired acoustic signal measurements are beamformed, and then signals corresponding to each boundary are calculated. Acoustic attenuation during the signal propagation is also compensated. In this equation, the unknowns are the subject's liver tissue properties and the electric field strengths. The electric field distribution, even at other tissues, is affected by the electrical properties of the liver. Equation (4) can be simply rewritten as a function of liver fat as follows:

$$\eta = f(\zeta), \quad (5)$$

where η is the rearranged term independent of the liver fat content ζ. The liver fat content can then be estimated by solving the following optimization problem:

$$\hat{\zeta} = \underset{\zeta \subseteq [0, LFF_{max}]}{\operatorname{argmin}} \ |\eta - f(\zeta)|^2, \quad (6)$$

where LFF_{max} is the maximum expected liver fat fraction, which was assumed to be 40%.